Proceedings of the ASME 2010 3rd Joint US-European Fluids Engineering Summer Meeting and 8th International Conference on Nanochannels, Microchannels, and Minichannels
FEDSM-ICNMM2010
August 1-5, 2010, Montreal, Canada

FEDSM-ICNMM2010-30518

TRANSPORT OF RESOLVED TURBULENT STRESSES IN A SPANWISE ROTATING CHANNEL FLOW

Qian-Qiu Xun, Bing-Chen Wang*
Dept. of Mechanical & Manufacturing Engineering
University of Manitoba
Winnipeg, MB, R3T 5V6, Canada
umxunq@cc.umanitoba.ca, bc_wang@umanitoba.ca

Gang Yan
School of Energy & Power Engineering
Xi'an Jiaotong University
Xi'an, Shaanxi, 710049, China
gyan@mail.xjtu.edu.cn

ABSTRACT

In this paper, we investigate the transport of resolved turbulent stresses in a plane channel flow subjected to spanwise rotation using the method of large-eddy simulation (LES). We present both the general and simplified transport equations for the resolved turbulent stresses, which are essential for understanding the unique pattern of turbulent kinetic energy production in a rotating system. Numerical simulations are performed using a dynamic nonlinear model (DNM) for closure of the filtered momentum equation. The turbulent flow field studied in this research is characterized by a Reynolds number $Re_\tau = 150$ and various rotation numbers Ro_τ ranging from 0 to 7.5. In order to validate the LES approach, turbulent statistics obtained from the simulations are thoroughly compared with the available experimental and direct numerical simulation results.

NOMENCLATURE

C_S, C_W, C_N SGS stress model coefficients
L_1, L_2, L_3 channel length, height, and width, respectively
$\mathcal{L}_{ij}$ Leonard type stress tensor
M_{ij}, W_{ij}, N_{ij} differential tensors
p pressure
Re_τ Reynolds number based on wall friction velocity: $u_\tau\delta/\nu$
Ro_τ rotation number: $2\Omega\delta/u_\tau$
$\bar{S}_{ij}$ resolved strain rate tensor: $(\partial\bar{u}_i/\partial x_j + \partial\bar{u}_j/\partial x_i)/2$
$|\bar{S}|$ norm of $\bar{S}_{ij}$: $(2\bar{S}_{ij}\bar{S}_{ij})^{1/2}$
s dimensionless parameter: $-2\Omega/(d\langle\bar{u}_1\rangle/dx_2)$
u_i velocity components: $i = 1, 2, 3$
u_τ wall friction velocity
α_{ij}, λ_{ij}, ζ_{ij} base stress tensor functions at the test-grid level
β_{ij}, γ_{ij}, η_{ij} base stress tensor functions at the grid level
δ half channel height
δ_{ij} Kronecker delta
Δ mesh or filter size
ε_{ijk} Levi-Civita symbol
ν kinematic viscosity
Ω angular velocity
$\bar{\Omega}_{ij}$ resolved rotation rate tensor: $(\partial\bar{u}_i/\partial x_j - \partial\bar{u}_j/\partial x_i)/2$
ρ density
τ_w wall shear stress
τ_{ij} grid-level SGS stress tensor
$(\cdot)_1$, $(\cdot)_2$, $(\cdot)_3$ streamwise, wall-normal, and spanwise components, respectively
$(\cdot)_p$ quantity near pressure side
$(\cdot)_s$ quantity near suction side
$(\cdot)_{ij}$ second-order tensor: $i, j = 1, 2, 3$
$(\cdot)^*_{ij}$ trace-free tensor: $(\cdot)^*_{ij} = (\cdot)_{ij} - (\cdot)_{kk}\delta_{ij}/3$
$(\cdot)_w$ value at the wall
$(\bar{\cdot})$ grid level filter; or resolved quantity
$(\tilde{\cdot})$ test-grid level filter
$[\cdot]$ ensemble-averaged quantity
$\langle\cdot\rangle$ time- and plane-averaged quantity

*Address all correspondence to this author.

INTRODUCTION

Turbulent flows subjected to a system rotation are of considerable interest in a variety of engineering, geophysical and astrophysical applications. The prediction and analysis of the effects of rotation on a flow field is critically important in designing high-performance rotating devices such as the internal blade cooling system in gas turbines, rotary compressors, multi-stage cyclone separators, centrifugal pumps and rotating heat exchangers. The Reynolds numbers for the flow in these engineering rotating devices are typically high, and the mean flow and turbulence level are affected by the Coriolis and centrifugal forces associated with the system rotation. In response to the Coriolis and centrifugal forces, large secondary flows are induced which dramatically alter the turbulent flow structures. As a consequence, the physical mechanisms underlying the transport of momentum in rotating flows are subject to further dynamical complexities, which impose additional challenges on the predictive accuracy of turbulence models.

The effects of rotation on the flow field in a plane channel can be quantified by a parameter $s \stackrel{\text{def}}{=} -2\Omega/(d\langle\bar{u}_1\rangle/dx_2)$. As shown in Fig. 1, the system is rotating in the spanwise direction with an angular velocity Ω (which is a positive constant in this study). According to the conventional stability criterion [1–3], the effect of rotation is destabilizing if $-1 < s < 0$, and stabilizing if $s > 0$. Tritton [4] has elaborated on this issue using a 'displaced particle analysis', although his research was related to the stability of laminar shear flows rather than turbulent flows. More specifically, turbulent mixing is enhanced on the side of the channel where the streamwise momentum is unstably stratified (this side being referred to also as the destabilized or pressure side), whereas turbulent mixing is reduced on the opposite side of the channel where the streamwise momentum is stably stratified (this side being referred to also as the stabilized or suction side). The terms 'destabilized' and 'stabilized' sides refer to the action of the Coriolis instability on the shear layers on the two sides of a channel. Owing to the existence of the Coriolis force, the mean streamwise velocity is larger on the stabilized side than on the destabilized side, and correspondingly, the static pressure decreases on the stabilized side and increases on destabilized side. As a result, the flow on the destabilized (pressure) side tends to become more turbulent and the boundary-layer tends to become thinner, whereas the flow on the stabilized (suction) side tends to become more laminarized and the boundary-layer tends to become thicker. These physical phenomena are of fundamental interest and have been reported in a variety of experimental and numerical studies [1, 3, 5–9].

In their experimental study of a rotating channel flow, Johnston *et al.* [1] observed large longitudinal roll cells associated with the secondary flow induced by the Coriolis force on the pressure side of the channel, whereas a nearly total suppression of turbulence was observed on the suction side. These large longitudinal roll cells appear in pairs and are interpreted as Taylor-Görtler (T-G) vortices analogous to those arising from the centrifugal instability mechanism associated with streamline curvature [10–12]. Unfortunately, as indicated by Johnston *et al.* [1], laboratory investigations of turbulence in a rotating channel can be challenging because it is difficult to achieve the fully-developed flow condition within a finite laboratory space.

Direct numerical simulations (DNS) and large-eddy simulations (LES) have been used to provide deeper physical insights into the effects of rotation on turbulence [3, 5–9]. Based on their DNS study, Kristoffersen and Andersson [3] pointed out that the T-G vortices are intrinsically unstable and are free to wander in the spanwise direction. Furthermore, these researchers developed an approximate correlation between the number of the T-G vortex pairs and the aspect ratio of the computational domain. Wu and Kasagi [13, 14] studied turbulent channel flow under an arbitrary directional system rotation using DNS. They found that the effect of spanwise rotation dominates the entire channel if spanwise rotation exists with comparable streamwise rotation or comparatively weak wall-normal rotation simultaneously. Furthermore, Wu and Kassagi [13, 14] observed that the combined action of streamwise and wall-normal rotation results in effects that are similar to that of spanwise rotation. Miyake and Kajishima [15,16] investigated the effect of the Coriolis force on the mean flow and turbulent structures using a LES method. However, the size of the computational domain in their numerical study was too small, and inevitably, their LES failed to reproduce one single persistent pair of T-G vortices.

Turbulent stress components under the influence of the Coriolis force play a significant role in the transport of the turbulent kinetic energy (TKE) and the interactions between small-scale flow structures. As demonstrated by Johnston *et al.* [1], the parameter s is actually the ratio of the production due to the rotational stresses to that due to the mean shear stresses. The DNS study of Kristoffersen and Andersson [3] further confirmed that the production terms associated with the Coriolis force have a significant influence on the absolute value and the distribution of both the normal and shear components of the turbulent stress. In this paper, we will present both the general and simplified transport equations for the resolved turbulent stresses in the context of LES, and report thoroughly the effects of spanwise system rotations on the transport of the resolved TKE.

To date, the novel dynamic nonlinear model (DNM) proposed by Wang and Bergstrom [17] for modelling the subgrid-scale (SGS) stress tensor has only been tested using a few canonical test cases such as Couette and Poiseuille flows, and mixed natural and forced convection flows in horizontal and vertical channels [17–20]. In this paper, we further aim at examining the predictive performance of this advanced dynamic nonlinear SGS stress model in the context of a new type of the body force (i.e., the Coriolis force) in a rotating channel flow.

SGS STRESS MODEL

In LES, the filtered continuity and momentum equations take the following form for an incompressible flow in a domain subjected to a system rotation:

$$\frac{\partial \bar{u}_i}{\partial x_i} = 0 \tag{1}$$

$$\frac{\partial \bar{u}_i}{\partial t} + \frac{\partial}{\partial x_j}(\bar{u}_i \bar{u}_j) = -\frac{1}{\rho}\frac{\partial \bar{p}}{\partial x_i} + \nu \frac{\partial^2 \bar{u}_i}{\partial x_j \partial x_j} - \frac{\partial \tau_{ij}}{\partial x_j} + 2\varepsilon_{ij3}\Omega \bar{u}_j \tag{2}$$

where $\bar{p}$ represents the effective pressure combined with the centrifugal force, ε_{ijk} is the Levi-Civita symbol. In this paper, we use x_1, x_2 and x_3 to denote the streamwise, wall-normal and spanwise coordinates, respectively (see Fig. 1). The last term on the right hand side of Eqn. (2) represents the Coriolis force term induced by a spanwise system rotation. As a consequence of the filtering process, the so-called SGS stress tensor appears in the above filtered momentum equation and is defined as $\tau_{ij} \stackrel{\text{def}}{=} \overline{u_i u_j} - \bar{u}_i \bar{u}_j$. The SGS stress tensor needs to be modeled in order to close the above system of governing equations.

In this study, the dynamic nonlinear model (DNM) of Wang and Bergstrom [17] is used to conduct our numerical simulations. The constitutive relation for the DNM is based on an explicit nonlinear quadratic tensorial polynomial constitutive relation originally proposed by Speziale [21] (see also Gatski and Speziale [22]) for modelling of the Reynolds stress tensor in a Reynolds-averaged Navier-Stokes (RANS) approach. By analogy, the SGS stress tensor can be modelled using the following functional form within the context of a LES approach:

$$\tau^*_{ij} = -C_S \beta_{ij} - C_W \gamma_{ij} - C_N \eta_{ij} \tag{3}$$

where an asterisk represents a trace-free tensor, i.e. $(\cdot)^*_{ij} \stackrel{\text{def}}{=} (\cdot)_{ij} - (\cdot)_{kk}\delta_{ij}/3$, and the base tensor functions are defined as $\beta_{ij} \stackrel{\text{def}}{=} 2\bar{\Delta}^2 |\bar{S}| \bar{S}_{ij}$, $\gamma_{ij} \stackrel{\text{def}}{=} 4\bar{\Delta}^2(\bar{S}_{ik}\bar{\Omega}_{kj} + \bar{S}_{jk}\bar{\Omega}_{ki})$ and $\eta_{ij} \stackrel{\text{def}}{=} 4\bar{\Delta}^2(\bar{S}_{ik}\bar{S}_{kj} - \bar{S}_{mn}\bar{S}_{nm}\delta_{ij}/3)$. Here, $\bar{\Delta}$ is the grid-level filter width; δ_{ij} is the Kronecker delta; $\bar{S}_{ij} \stackrel{\text{def}}{=} (\partial \bar{u}_i/\partial x_j + \partial \bar{u}_j/\partial x_i)/2$ and $\bar{\Omega}_{ij} \stackrel{\text{def}}{=} (\partial \bar{u}_i/\partial x_j - \partial \bar{u}_j/\partial x_i)/2$ are the resolved strain and rotation rate tensors, respectively; and, $|\bar{S}| = (2\bar{S}_{ij}\bar{S}_{ij})^{1/2}$ is the norm of the resolved strain rate tensor. It can be shown [17] that the values of the three model coefficients C_S, C_W and C_N can be obtained by minimizing the residual of the Germano identity following the dynamic procedure of Lilly [23], viz.

$$\begin{bmatrix} M_{ij}M_{ij} & M_{ij}W_{ij} & M_{ij}N_{ij} \\ W_{ij}M_{ij} & W_{ij}W_{ij} & W_{ij}N_{ij} \\ N_{ij}M_{ij} & N_{ij}W_{ij} & N_{ij}N_{ij} \end{bmatrix} \cdot \begin{bmatrix} C_S \\ C_W \\ C_N \end{bmatrix} = - \begin{bmatrix} \mathcal{L}^*_{ij}M_{ij} \\ \mathcal{L}^*_{ij}W_{ij} \\ \mathcal{L}^*_{ij}N_{ij} \end{bmatrix} \tag{4}$$

where $\mathcal{L}_{ij} \stackrel{\text{def}}{=} \widetilde{\bar{u}_i \bar{u}_j} - \tilde{\bar{u}}_i \tilde{\bar{u}}_j$ is the resolved Leonard type stress; $M_{ij} \stackrel{\text{def}}{=} \alpha_{ij} - \tilde{\beta}_{ij}$, $W_{ij} \stackrel{\text{def}}{=} \lambda_{ij} - \tilde{\gamma}_{ij}$ and $N_{ij} \stackrel{\text{def}}{=} \zeta_{ij} - \tilde{\eta}_{ij}$ are differential tensors, respectively; and $\alpha_{ij} \stackrel{\text{def}}{=} 2\tilde{\bar{\Delta}}^2 |\tilde{\bar{S}}| \tilde{\bar{S}}_{ij}$,

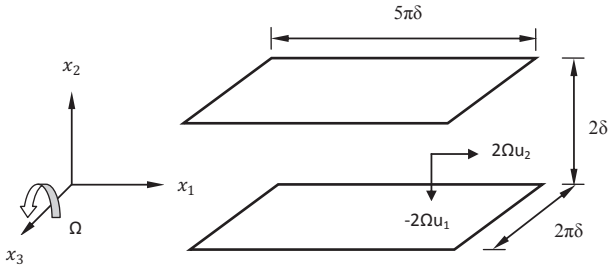

FIGURE 1. COMPUTATIONAL DOMAIN FOR A SPANWISE ROTATING CHANNEL FLOW. SPECIFIC TO THIS ROTATING CHANNEL FLOW, THE PRESSURE (DESTABILIZING) SIDE WALL IS LOCATED AT $x_2/\delta = -1.0$, AND THE SUCTION (STABILIZING) SIDE WALL IS LOCATED AT $x_2/\delta = 1.0$.

$\lambda_{ij} \stackrel{\text{def}}{=} 4\tilde{\bar{\Delta}}^2(\tilde{\bar{S}}_{ik}\tilde{\bar{\Omega}}_{kj} + \tilde{\bar{S}}_{jk}\tilde{\bar{\Omega}}_{ki})$ and $\zeta_{ij} \stackrel{\text{def}}{=} 4\tilde{\bar{\Delta}}^2(\tilde{\bar{S}}_{ik}\tilde{\bar{S}}_{kj} - \tilde{\bar{S}}_{mn}\tilde{\bar{S}}_{nm}\delta_{ij}/3)$ are test-grid level base tensor functions. Here, quantities filtered at the grid level are denoted using an overbar and those filtered at the test-grid level are denoted using a tilde.

The design of the constitutive relation of Eqn. (3), in terms of the choice of the three constituent tensorial base components (i.e., β_{ij}, γ_{ij} and η_{ij}) is not arbitrary: (i) the first term β_{ij} is the well-known Smagorinsky component which primarily relates to the SGS dissipation and forward scatter of kinetic energy (KE) from the resolved to subgrid scale motions; (ii) the second term γ_{ij} does not make any contribution to the KE transfer between the resolved and subgrid scales, but according to a recent systematic *a priori* LES study of Horiuti [24], it significantly improves the correlation between the exact τ_{ij} extracted from a DNS database and that predicted by the nonlinear model; and, (iii) as demonstrated previously [17, 19, 20], the third term η_{ij} contributes significantly to the backscatter of KE from the subgrid to the resolved scales. The three features mentioned here are among the most important criteria for evaluation of a SGS stress model. Speziale's constitutive relation on which the DNM is based, offers an effective representation to model individually these three important physical features using three independent terms. Further successful applications of the DNM can be found in Wang *et al.* [19] on the study of the topological features of wall-bounded turbulent flows, in [25, 26] on the study the geometrical properties of the SGS stress tensor and resolved vorticity vector, and in [20] on the study of an unstably stratified turbulent channel flow.

TEST CASE AND NUMERICAL ALGORITHM

Figure 1 shows the computational domain of the rotating plane channel and coordinate system used in the numerical simulation. The plane channel rotates with a constant positive angular velocity, Ω, parallel to the x_3 direction. Because this research focuses on examining the rotation effects on the resolved turbulent stresses, only one Reynolds number will be used in this paper;

and for this fixed Reynolds number, a series of different rotation numbers representing a wide range of angular velocities will be thoroughly tested and compared. The flow is characterized by a Reynolds number of $Re_\tau \stackrel{\text{def}}{=} u_\tau \delta/\nu = 150$ and various rotation numbers Ro_τ ranging from 0 to 7.5. The dimensions of the computational domain are $L_1 \times L_2 \times L_3 = 5\pi\delta \times 2\delta \times 2\pi\delta$ in the streamwise (x_1), wall-normal (x_2) and spanwise (x_3) directions, respectively. Characteristic of a conventional implicit filtering LES approach, the levels of the resolved and subgrid scale components in a numerical simulation rely on the filter size at the grid level (which is also the characteristic size of a control volume). A grid system with $48 \times 32 \times 48$ control volumes is used to discretize the computational domain. The grid is uniform in the streamwise and spanwise directions, and stretched in the wall-normal direction using a hyperbolic-tangent function in order to provide a greater resolution in the near-wall region.

A finite volume method based on a collocated grid system was applied to the discretization of the governing equations. The nonlinear advection term was discretized using a second-order explicit Adams-Bashforth scheme and the viscous diffusion term was discretized using a second-order Crank-Nicolson scheme [27]. A second-order central difference scheme was applied for the spatial discretization as it represents a good compromise between accuracy, simplicity and efficiency [28]. At each time step, the pressure field was updated by solving a Poisson type pressure correction equation using a multi-grid method. The checkerboard effect in the pressure field arising from the pressure-velocity decoupling on a collocated grid system was removed using a nonlinear momentum interpolation scheme [29] for the evaluation of cell-face velocities from the nodal values.

No slip and impermeable boundary conditions are imposed on the velocity components at the walls. Periodic boundary conditions are employed in the streamwise and spanwise directions since the flow and temperature fields are assumed to be statistically homogeneous in both these directions. Statistics of various flow variables are calculated based on 80,000 time steps after the fluid field has become turbulent and fully-developed.

In the presentation of the numerical results, quantities non-dimensionalized using the wall friction velocity $u_\tau \stackrel{\text{def}}{=} \sqrt{\tau_w/\rho}$ are denoted with a superscript '+'.

MEAN RESOLVED VELOCITY PROFILES

In order to validate the numerical approach, the LES results obtained from the simulations are compared with the DNS data of Nishimura and Kasagi [30] (designated as NK-1996) for a rotating channel flow under the same operating conditions. In addition, a set of DNS data on non-rotating channel flows ($Ro_\tau = 0$) obtained by Iwamoto *et al.* [31] (designated as ISK-2002) are also used in our comparative study.

Figure 2 show the mean resolved streamwise velocity profiles in the wall-normal direction across the channel. As shown in Fig. 2, the mean velocity profile is symmetric about the central channel plane ($x_2/\delta = 0$) for the non-rotating case ($Ro_\tau = 0$). However, for the rotating case tested, it is evident from Fig. 2 that $d\langle\bar{u}_1\rangle/dx_2 > 0$ holds in the region near the pressure side (i.e., at $x_2/\delta = -1.0$), which results in $s < 0$, indicating that the system rotation has a destabilizing effect on the flow field. In contrast, near the suction side (i.e., at $x_2/\delta = 1.0$), $d\langle\bar{u}_1\rangle/dx_2 < 0$, a condition that results in $s > 0$, indicating that system rotation has a stabilizing effect on the flow field. Here $\langle\cdot\rangle$ corresponds to a quantity averaged both in time and over the homogeneous (x_1, x_3)-plane. The wall shear stress of the rotating channel flow is enhanced near the pressure side and reduced near the suction side because $|d\langle\bar{u}_1\rangle/dx_2|_{wp} > |d\langle\bar{u}_1\rangle/dx_2|_{ws}$ (which is evident in Fig. 2 by comparing the values of $|d\langle\bar{u}_1\rangle/dx_2|_w$ for the rotating and non-rotating cases). This phenomenon is typically referred to as the 'Ekman layer effect', and is caused by the balance between the Coriolis force, mean pressure gradient and turbulent drag in a layer of flow subjected to a system rotation. Owing to the existence of the Coriolis force, large T-G vortices are induced in the core region of the channel, which shift the mean velocity profiles to the pressure side. Consequently, the momentum viscous sublayer becomes thinner on the pressure side and becomes thicker on the suction side. In the above discussion, the subscript 'w' is used to indicate the value of a variable at the channel wall, and the modifying subscripts 'p' and 's' are used to denote the region near pressure and suction side, respectively.

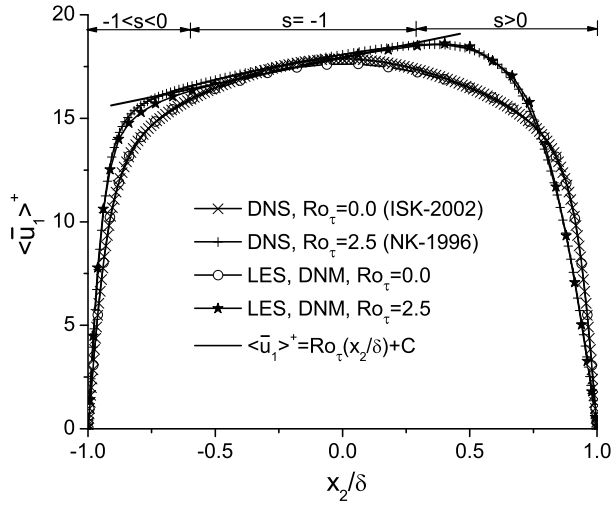

FIGURE 2. PROFILES OF THE MEAN RESOLVED STREAMWISE VELOCITY AT $Ro_\tau = 0$ AND 2.5.

From previous studies [1, 3], it is known that a relationship $s = -2\Omega/(d\langle\bar{u}_1\rangle/dx_2) = -1$ holds in the core region of a rotating channel, implying that the value of the mean shear vorticity component $d\langle\bar{u}_1\rangle/dx_2$ approaches 2Ω. As such, the absolute mean vorticity becomes approximately zero in the core region of

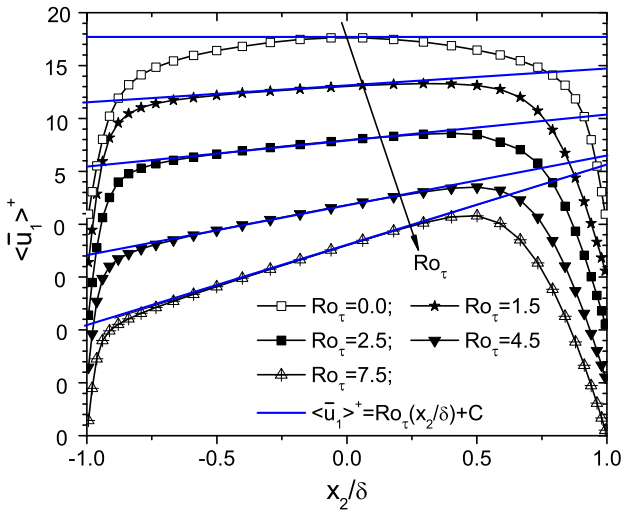

FIGURE 3. PROFILES OF THE MEAN RESOLVED STREAMWISE VELOCITY AT VARIOUS ROTATION NUMBERS.

the channel, i.e.

$$2\Omega - d\langle \bar{u}_1 \rangle / dx_2 \approx 0 \tag{5}$$

This particular portion of the velocity profile corresponds to a flow region of neutral stability [3]. The neutral stability relationship represented by Eqn. (5) can be further integrated and written in a dimensionless form, viz.

$$\langle \bar{u}_1 \rangle^+ = Ro_\tau \cdot \frac{x_2}{\delta} + C \tag{6}$$

where C is a constant of integration.

As shown in Fig. 3, the mean resolved streamwise velocity profile becomes increasingly asymmetric as the rotation number increases. In the core region, the profiles become approximately linear with slope Ro_τ when rotation is imposed. Furthermore, the width of the neutral stability zone in the central core of the channel increases as Ro_τ increases from 0 to 7.5. These findings are fully consistent with the laboratory measurements of Johnston *et al.* [1] and the DNS predictions of Kristoffersen and Andersson [3].

TRANSPORT OF RESOLVED TURBULENT STRESSES AND TKE

An instantaneous filtered quantity can be decomposed into a time- and plane-averaged component and a residual component as:

$$\bar{\phi} = \langle \bar{\phi} \rangle + \bar{\phi}'' \tag{7}$$

Based on this method of the decomposition, the predicted resolved velocity fluctuations (or root-mean-square (RMS) values) can be defined as

$$\bar{u}^+_{i,rms} \overset{\text{def}}{=} \left\langle \left(\frac{\bar{u}_i - \langle \bar{u}_i \rangle}{u^a_\tau} \right)^2 \right\rangle^{1/2} = \frac{\langle \bar{u}''^2_i \rangle^{1/2}}{u^a_\tau} \tag{8}$$

TABLE 1. PRODUCTION TERMS DUE TO THE MEAN TURBULENT SHEAR (P_{ij}) AND ROTATIONAL (G_{ij}) STRESSES FOR A FULLY-DEVELOPED ROTATING PLANE CHANNEL FLOW.

ij	11	22	33	12
P_{ij}	$-2\langle \bar{u}''_1 \bar{u}''_2 \rangle (d\langle \bar{u}_1 \rangle / dx_2)$	0	0	$\langle \bar{u}''^2_2 \rangle (d\langle \bar{u}_1 \rangle / dx_2)$
G_{ij}	$4\Omega \langle \bar{u}''_1 \bar{u}''_2 \rangle$	$-4\Omega \langle \bar{u}''_1 \bar{u}''_2 \rangle$	0	$2\Omega(\langle \bar{u}''^2_1 \rangle - \langle \bar{u}''^2_2 \rangle)$

for $i = 1$, 2 and 3 respectively, where $u^a_\tau = (u_{\tau p} + u_{\tau s})/2$ is the averaged wall friction velocity over both the pressure and suction side.

The effects of the Coriolis force on the resolved turbulent stresses and TKE can be further studied through their transport equations, which are derived and documented in Appendix A. As revealed in the experimental study of Johnston *et al.* [1] and DNS study of Kristoffersen and Andersson [3], the production terms in the transport equations of the resolved turbulent stresses (cf. Eqs. (21)–(24) in Appendix A) have a significant influence on the absolute value and distribution of the resolved turbulent shear stresses (i.e., $-[\bar{u}''_i \bar{u}''_k]$ or $-\langle \bar{u}''_i \bar{u}''_k \rangle$) and TKE (i.e., $\frac{1}{2}[\bar{u}''_i \bar{u}''_i]$ or $\frac{1}{2}\langle \bar{u}''_i \bar{u}''_i \rangle$). Here, the operator $[\cdot]$ represents ensemble-averaging (whereas, $\langle \cdot \rangle$ represents time- and plane-averaging). From Eqn. (23), the production of the resolved shear stress component $-\langle \bar{u}''_1 \bar{u}''_2 \rangle$ in a fully-developed rotating channel is given by

$$\langle P_{12} \rangle + \langle G_{12} \rangle = \langle \bar{u}''^2_2 \rangle \frac{d\langle \bar{u}_1 \rangle}{dx_2} + 2\Omega(\langle \bar{u}''^2_1 \rangle - \langle \bar{u}''^2_2 \rangle) \tag{9}$$

and those of the normal stress components in the three coordinate directions $\langle \bar{u}''_k \bar{u}''_k \rangle$ (no summation implied here, see Eqn. (24)) are given by

$$\langle P_{11} \rangle + \langle G_{11} \rangle = -2\langle \bar{u}''_1 \bar{u}''_2 \rangle \frac{d\langle \bar{u}_1 \rangle}{dx_2} + 4\Omega \langle \bar{u}''_1 \bar{u}''_2 \rangle \tag{10}$$

$$\langle P_{22} \rangle + \langle G_{22} \rangle = 0 - 4\Omega \langle \bar{u}''_1 \bar{u}''_2 \rangle \tag{11}$$

$$\langle P_{33} \rangle + \langle G_{33} \rangle = 0 + 0 \tag{12}$$

The first term on both the left hand side (LHS) and the corresponding right hand side (RHS) of Eqns. (9)-(12) represents the production term arising from the mean resolved turbulent (shear and normal) stresses. The second term on the LHS and the corresponding RHS of Eqns. (9)-(12) represents the rotational stress production term that arises from the presence of Coriolis accelerations in a rotating channel flow. To facilitate the interpretation of the results in Figs. 4-7, Eqns. (9)-(12) are written in component forms in Tab. 1. It is worthwhile to note that in a non-rotating case ($Ro_\tau = 0$), $-\langle \bar{u}''_1 \bar{u}''_2 \rangle$ has the same parity as $d\langle \bar{u}_1 \rangle / dx_2$, both of which are positive and negative for $x_2 < 0$ and $x_2 > 0$, respectively. This implies that $P_{11} > 0$ holds across the entire channel, whereas P_{12} assumes a sign that is opposite to that

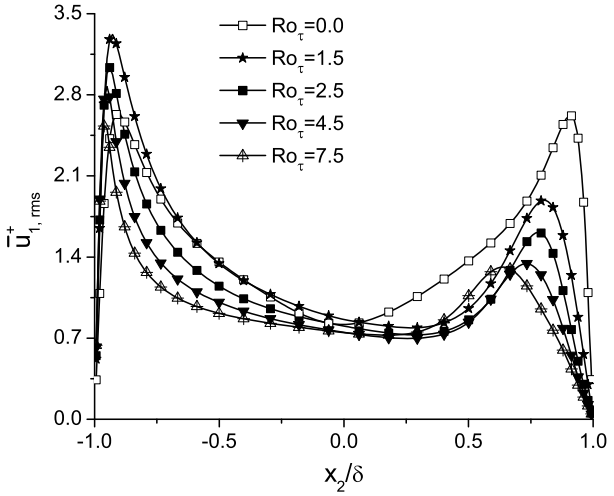

FIGURE 4. RESOLVED RMS OF THE STREAMWISE VELOCITY AT VARIOUS ROTATION NUMBERS.

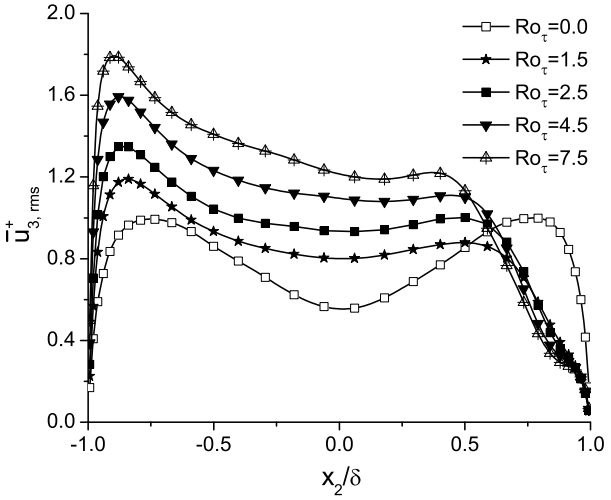

FIGURE 6. RESOLVED RMS OF THE SPANWISE VELOCITY AT VARIOUS ROTATION NUMBERS.

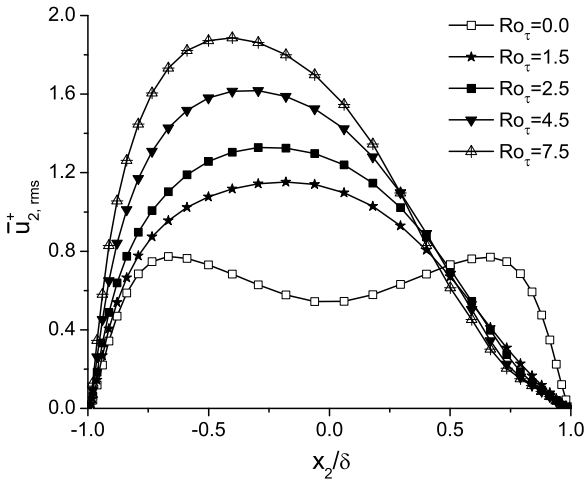

FIGURE 5. RESOLVED RMS OF THE WALL-NORMAL VELOCITY AT VARIOUS ROTATION NUMBERS.

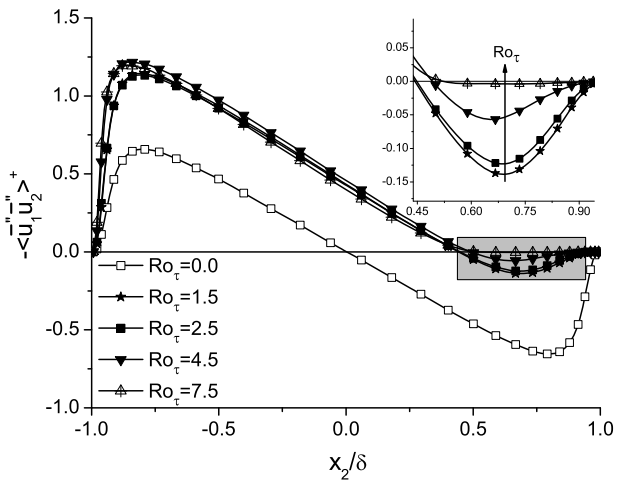

FIGURE 7. RESOLVED TURBULENT SHEAR STRESS AT VARIOUS ROTATION NUMBERS.

of x_2. However, due to the asymmetry of the resolved streamwise velocity profile in the wall-normal direction, this statement does not strictly hold for a rotating channel flow. Because $P_{22} = P_{33} = 0$, there is no direct production of either $\langle \bar{u}_2''^2 \rangle$ or $\langle \bar{u}_3''^2 \rangle$ from the resolved turbulent stresses. However energy redistributes within the system and influences both these terms through the mechanisms of molecular diffusion, SGS production and diffusion, and pressure-strain interactions (see Eqn. (24)).

Characteristics of the Suction Side

Near the suction wall (located at $x_2/\delta = 1$) of the channel, the direct effects of system rotation are expected to reduce $\langle \bar{u}_2''^2 \rangle$ (or $\bar{u}_{2,rms}$) because $G_{22} < 0$. As shown in Fig. 5, the value of $\bar{u}_{2,rms}$ is indeed damped considerably in the region close to the suction wall, and the near-wall peak in the profile of $\bar{u}_{2,rms}$ characteristic of a non-rotating channel disappears in all four rotating channel cases tested. Near the suction wall, $-\langle \bar{u}_1'' \bar{u}_2'' \rangle < 0$, and the two production terms $G_{12} > 0$ and $P_{12} < 0$ (because $d\langle \bar{u}_1 \rangle / dx_2 < 0$, see Fig. 3). Because the value of $\langle \bar{u}_2''^2 \rangle$ is significantly reduced as the suction wall is approached, the value of $|G_{12}|$ increases whereas that of $|P_{12}|$ decreases. Consequently, the level of the total production $P_{12} + G_{12}$ for the turbulent shear stress $-\langle \bar{u}_1'' \bar{u}_2'' \rangle$ increases, which then results in an increase in the value of $-\langle \bar{u}_1'' \bar{u}_2'' \rangle$ (correspondingly, a reduction in its magnitude $|-\langle \bar{u}_1'' \bar{u}_2'' \rangle|$) on the suction side. This physical feature that the magnitude of $-\langle \bar{u}_1'' \bar{u}_2'' \rangle$ is damped by the imposed system rotation in the flow region near the suction wall is evident in Fig. 7.

As shown in Fig. 4, the level of $\bar{u}_{1,rms}$ decreases monotonically with Ro_τ on the suction side. The physical mechanism underlying this phenomenon can be explained as follows. On the suction side, $P_{11} > 0$ and $G_{11} > 0$. As pointed out by Kristoffersen and Andersson [3], the ratio of G_{11}/P_{11} attains positive values appreciably below unity near the suction side of a rotating channel. Therefore, the total production $P_{11}+G_{11} = (1+s)P_{11}$ is dominated by the mean turbulent shear production P_{11}. Furthermore, as Ro_τ increases, P_{11} decreases monotonically because both magnitudes of the turbulent shear stress $|-\langle\bar{u}_1''\bar{u}_2''\rangle|$ and the mean velocity gradient $|d\langle\bar{u}_1\rangle/dx_2|$ decrease monotonically (see Fig. 3). In view of this, the value of $\langle\bar{u}_1''^2\rangle$ decreases monotonically as Ro_τ increases in the flow region close to the suction wall.

Although $P_{33} = G_{33} = 0$, the profiles of $\bar{u}_{3,rms}$ (or, $\langle\bar{u}_3''^2\rangle$) in Fig. 6 show that the resolved turbulent normal stress in the spanwise direction is still significantly affected by rotation. Since both $\langle\bar{u}_1''^2\rangle$ and $\langle\bar{u}_2''^2\rangle$ are reduced by system rotation on the suction side, less energy becomes available for redistribution to alter the level of $\langle\bar{u}_3''^2\rangle$ through the processes associated with molecular diffusion, SGS production and diffusion, and pressure-strain correlations. Another noticeable feature exhibited in Figs. 4-7 is that the near-wall peak that is characteristic of $\langle\bar{u}_1''^2\rangle$, $\langle\bar{u}_3''^2\rangle$ and $-\langle\bar{u}_1''\bar{u}_2''\rangle$ is shifted away from the suction side towards the center of the channel. This observation corresponds to the physics that as Ro_τ increases, the suction side tends to become more laminarized resulting in a thicker Ekman layer.

Characteristics of the Pressure Side

On the pressure side of the channel, both the resolved turbulent shear stress $-\langle\bar{u}_1''\bar{u}_2''\rangle$ and mean streamwise velocity gradient $d\langle\bar{u}_1\rangle/dx_2$ are positive. The rotational stress production terms, $G_{22} = -G_{11} > 0$ and $G_{12} > 0$, tend to increase $\langle\bar{u}_2''^2\rangle$ and $-\langle\bar{u}_1''\bar{u}_2''\rangle$, and to reduce $\langle\bar{u}_1''^2\rangle$. The mean turbulent shear production P_{11} is, however, indirectly enhanced by the increase in the resolved turbulent shear stress, thereby resulting in a net enhancement of $\langle\bar{u}_1''^2\rangle$ (as the ratio $|s| = |G_{11}/P_{11}| < 1$ holds near the pressure side). Furthermore, because $P_{22} + G_{22} = G_{22} \propto \Omega > 0$, it is anticipated that the level of $\langle\bar{u}_2''^2\rangle$ (or $\bar{u}_{2,rms}$) increases monotonically with Ro_τ on the pressure side. The distributions of the resolved turbulent stresses shown in Figs. 4-7 are generally in agreement with these expectations, and are also consistent with the DNS results of Kristoffersen and Andersson [3]. However, it should be stressed that the concept of the resolved turbulent shear stresses is different between a LES and a DNS approach (as represented by this research and that of Kristoffersen and Andersson [3], respectively).

As shown in Fig. 4, in comparison with the non-rotating case ($Ro_\tau = 0.0$), the level of $\langle\bar{u}_1''^2\rangle$ increases by approximately 50% at $Ro_\tau = 1.5$ in the near-wall region on the pressure side, and the level decreases as Ro_τ increases. As the rotation number

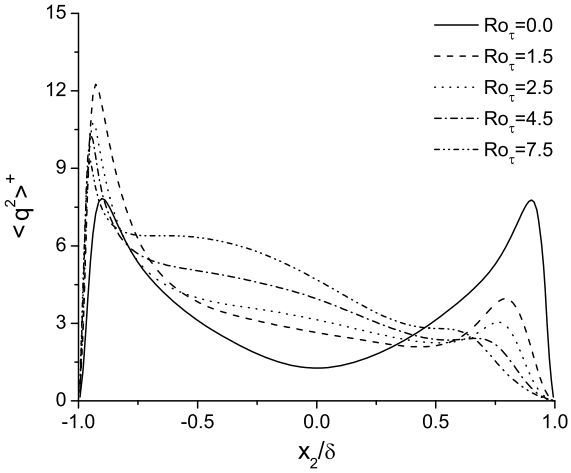

FIGURE 8. RESOLVED TURBULENT KINETIC ENERGY AT VARIOUS ROTATION NUMBERS, NON-DIMENSIONALIZED USING $(u_\tau^a)^2$.

increases, the irrotational zone where the neutral stability relationship $d\langle\bar{u}_1\rangle/dx_2 = 2\Omega$ holds, penetrates deeper into the boundary-layer of the pressure wall. In the neutral stability zone, $s = -1$ and therefore, the total production of $\langle\bar{u}_1''^2\rangle$ vanishes (i.e., $P_{11}+G_{11} = (1+s)P_{11} = 0$). The suppression of $\langle\bar{u}_1''^2\rangle$ and augmentation of $\langle\bar{u}_2''^2\rangle$ eventually make the positive rotational production term $G_{12} = 2\Omega(\langle\bar{u}_1''^2\rangle - \langle\bar{u}_2''^2\rangle)$ change its sign. At the highest rotation number $Ro_\tau = 7.5$, $\langle\bar{u}_2''^2\rangle$ exceeds $\langle\bar{u}_1''^2\rangle$ in the range $-0.75 < x_2/\delta < 0.25$ (which corresponds to a region that extends over 50% of the channel cross-section). This reversal of the turbulent stress anisotropy, which renders G_{12} being negative rather than positive, is responsible for preventing any further increase in $-\langle\bar{u}_1''\bar{u}_2''\rangle$ at higher rotation speeds in Fig. 7.

Rotation Effect on the Resolved TKE

The resolved TKE is defined as

$$\langle q^2\rangle = \frac{1}{2}(\langle\bar{u}_1''^2\rangle + \langle\bar{u}_2''^2\rangle + \langle\bar{u}_3''^2\rangle) \tag{13}$$

The production terms for $\langle q^2\rangle$ can be obtained by taking one half of the sum of Eqns. (10), (11) and (12), so

$$\langle P_{q^2}\rangle + \langle G_{q^2}\rangle = -\langle\bar{u}_1''\bar{u}_2''\rangle\frac{d\langle\bar{u}_1\rangle}{dx_2} + 0 \tag{14}$$

This equation clearly shows that the production of the resolved TKE is not explicitly dependent upon Ω, but rather is implicitly affected by the rotation through the effects of Ω on the resolved turbulent shear stress ($-\langle\bar{u}_1''\bar{u}_2''\rangle$) and mean viscous shear stress (indicated by $d\langle\bar{u}_1\rangle/dx_2$). From Eqn. (14), it is obvious that P_{q^2} is one-half of P_{11}, which is the production term for $\langle\bar{u}_1''^2\rangle$ (see discussions above). Therefore, it is anticipated that the resolved TKE $\langle q^2\rangle$ will also exhibit a behaviour similar to that of the

resolved streamwise turbulent normal stress component $\langle \bar{u}_1''^2 \rangle$. This expected pattern is evident on comparison of Fig. 8 with Fig. 4. On the pressure side, the peak value of $\langle q^2 \rangle$ increases by approximately 50% at $Ro_\tau = 1.5$ relative to that for the non-rotating case $Ro_\tau = 0$, and then decreases as Ro_τ increases. On the suction side, $\langle q^2 \rangle$ decreases monotonically as Ro_τ increases, indicating that the flow there becomes more laminarized at the higher rotation numbers.

CONCLUSIONS

The DNM [17] for modelling the SGS stress tensor was used to simulate a fully-developed rotating channel flow for different rotation numbers ranging from 0 to 7.5. The numerical results obtained from our simulations have been thoroughly validated against reported experimental measurements [1] and DNS data [3, 30, 31]. It is shown that large-eddy simulations based on the DNM can successfully predict the transport of resolved turbulent stresses in a rotating channel.

The secondary flow represented by the Taylor-Görtler vortices drastically alters the velocity fields. It is observed that the resolved mean velocity profiles shift from the suction side towards the pressure side, and the Ekman layer becomes thicker on the suction side as the rotation number increases. In the core region of the channel, the resolved mean streamwise velocity profile exhibits a linear behaviour with a slope that is proportional to 2Ω, reflecting the neutral stratification (or, stability) of the flow in this region.

As a new contribution to the current literature, the general and simplified transport equations for the resolved turbulent stresses are systematically derived in order to study the resolved second-order velocity statistics in the context of LES. The magnitude of the resolved turbulent stresses and TKE are influenced by two production terms, P_{ij} and G_{ij}, which are related to the turbulent shear and rotation stresses, respectively.

Near the suction side of the channel, the resolved streamwise turbulent intensity $\langle \bar{u}_1''^2 \rangle$, the magnitude of the resolved turbulent shear stress $|-\langle \bar{u}_1'' \bar{u}_2'' \rangle|$ and the resolved TKE $\langle q^2 \rangle$ decrease gradually as Ro_τ increases. The level of resolved wall-normal and spanwise turbulent intensities are damped considerably on the suction side. The near-wall peak that is characteristic of $\langle \bar{u}_1''^2 \rangle$, $\langle \bar{u}_3''^2 \rangle$, $-\langle \bar{u}_1'' \bar{u}_2'' \rangle$ and $\langle q^2 \rangle$ shifts away from the suction side towards the center of the channel, reflecting the physics that the suction side tends to become more laminarized resulting in a thicker Ekman layer as the rotation number Ro_τ increases.

In contrast, near the pressure side of the channel, turbulent intensities in the wall-normal and spanwise direction increase monotonically as the rotation number Ro_τ increases. The mean turbulent shear production P_{11} results in a net enhancement of $\langle \bar{u}_1''^2 \rangle$. In comparison with the non-rotating case ($Ro_\tau = 0$), the level of $\langle \bar{u}_1''^2 \rangle$ and $\langle q^2 \rangle$ increase by approximately 50% at $Ro_\tau = 1.5$ and then decreases as Ro_τ further increases. The magnitude of the resolved turbulent shear stress component $-\langle \bar{u}_1'' \bar{u}_2'' \rangle$ is significantly influenced by the rotational stress production term G_{12}. This reversal of the turbulent stress anisotropy, which renders G_{12} being negative rather than positive, is responsible for preventing any further increase in $-\langle \bar{u}_1'' \bar{u}_2'' \rangle$ at higher rotation speeds.

REFERENCES

[1] Johnston, J. P., Halleen, R. M., and Lezius, D. K., 1972. "Effects of spanwise rotation on the structure of two-dimensional fully developed turbulent channel flow". *J. Fluid Mech.,* ***56***, pp. 533–557.

[2] Bradshaw, P., 1969. "The analogy between streamline curvature and buoyancy in turbulent shear flow". *J. Fluid Mech.,* ***36***, pp. 177–191.

[3] Kristoffersen, R., and Andersson, H. I., 1993. "Direct simulations of low-reynolds-number turbulent flow in a rotating channel". *J. Fluid Mech.,* ***256***, pp. 163–197.

[4] Tritton, D. J., 1992. "Stabilization and destabilization of turbulent shear flow in rotating fluid". *J. Fluid Mech.,* ***241***, pp. 503–523.

[5] Pallares, J., and Davidson, L., 2002. "Large-eddy simulations of turbulent heat transfer in stationary and rotating square ducts". *Phys. Fluids,* ***14***, pp. 2804–2816.

[6] Pallares, J., Grau, F. X., and Davidson, L., 2005. "Pressure drop and heat transfer rates in forced convection rotating square duct flows at high rotation rates". *Phys. Fluids,* ***17***, pp. 1–11.

[7] Lamballais, E., Metais, O., and Lesieur, M., 1998. "Spectraldynamical model for large-eddy simulations of turbulent rotating channel flow". *Theor. Comput. Fluid Dyn.,* ***12***, pp. 149–177.

[8] Piomelli, U., and Liu, J., 1995. "Large-eddy simulation of rotating channel flows using a localized dynamic model". *Phys. Fluids,* ***7***, pp. 839–848.

[9] Li, B.-Y., Liu, N.-S., and Lu, X.-Y., 2006. "Direct numerical simulation of wall-normal rotating turbulent channel flow with heat transfer". *Int. J. Heat Mass Trans.,* ***49***, pp. 1162–1175.

[10] Hunt, I. A., and Joubert, P. N., 1979. "Effects of small streamline curvature on turbulent duct flow". *J. Fluid Mech.,* ***91***, pp. 633–659.

[11] Hoffmann, P. H., Muck, K. C., and Bradshaw, P., 1985. "The effect of concave surface curvature on turbulent boundary layers". *J. Fluid Mech.,* ***161***, pp. 371–403.

[12] Moser, R. D., and Moin, P., 1987. "The effects of curvature in wallbounded turbulent flows". *J. Fluid Mech.,* ***175***, pp. 479–510.

[13] Wu, H., and Kasagi, N., 2004. "Turbulent heat transfer in

a channel flow with arbitrary directional system rotation". *Int. J. Heat Mass Trans.,* ***47***, pp. 4579–4591.

[14] Wu, H., and Kasagi, N., 2004. "Effects of arbitrary directional system rotation on turbulent channel flow". *Phys. Fluids,* ***16***, pp. 979–990.

[15] Miyake, Y., and Kajishima, T., 1986. "Numerical simulation of the effects of coriolis force on the structure of turbulence (1st report, global effects)". *Bulletin JSME,* ***29***, pp. 3341–3346.

[16] Miyake, Y., and Kajishima, T., 1986. "Numerical simulation of the effects of coriolis force on the structure of turbulence (2nd report, structure of turbulence)". *Bulletin JSME,* ***29***, pp. 3347–3351.

[17] Wang, B.-C., and Bergstrom, D. J., 2005. "A dynamic nonlinear subgrid-scale stress model". *Phys. Fluids,* ***17***, pp. 1–15.

[18] Wang, B.-C., Yin, J., Yee, E., and Bergstrom, D. J., 2007. "A complete and irreducible dynamic sgs heat-flux modelling based on the strain rate tensor for large-eddy simulation of thermal convection". *Int. J. Heat Fluid Flow,* ***28***, pp. 1227–1243.

[19] Wang, B.-C., Yin, D. J. B. J., and Yee, E., 2006. "Turbulence topologies predicted using large eddy simulations". *J. Turbul.,* ***7***, pp. 1–28.

[20] Wang, B.-C., and Bergstrom, D. J., 2008. "Geometrical properties of the vorticity vector derived using large-eddy simulation". *Fluid Dyn. Res.,* ***40***, pp. 123–154.

[21] Speziale, C. G., 1987. "On nonlinear K–l and K–ϵ models of turbulence". *J. Fluid Mech.,* ***178***, pp. 459–475.

[22] Gatski, T. B., and Speziale, C. G., 1993. "On explicit algebraic stress models for complex turbulent flows". *J. Fluid Mech.,* ***254***, pp. 59–78.

[23] Lilly, D. K., 1992. "A proposed modification of the germano subgrid-scale closure method". *Phys. Fluids A,* ***4***, pp. 633–635.

[24] Horiuti, K., 2003. "Roles of non-aligned eigenvectors of strain-rate and subgrid-scale stress tensors in turbulence generation". *J. Fluid Mech.,* ***491***, pp. 65–100.

[25] Wang, B.-C., Yee, E., and Bergstrom, D. J., 2006. "Geometrical description of subgrid-scale stress tensor based on euler axis/angle". *AIAA J.,* ***44***, pp. 1106–1110.

[26] Wang, B.-C., Yee, E., Bergstrom, D. J., and Iida., O., 2008. "New dynamic subgrid-scale heat flux models for large-eddy simulation of thermal convection based on the general gradient diffusion hypothesis". *J. Fluid Mech.,* ***604***, pp. 125–163.

[27] Kim, J., and Moin, P., 1985. "Application of a fractional-step method to incompressible navier-stokes equations". *J. Comp. Phys.,* ***59***, pp. 308–323.

[28] Ferziger, J. H., and Perić, M., 1999. *Computational Methods for Fluid Dynamics*. Springer, Berlin.

[29] Rhie, C. M., and Chow, W. L., 1983. "Numerical study of the turbulent flow past an airfoil with trailing edge separation". *AIAA J.,* ***21***, pp. 1525–1532.

[30] Nishimura, M., and Kasagi, N., 1996. "Direct numerical simulation of combined forced and natural turbulent convection in a rotating plane channel". In Proc. 3rd KSME-JSME Therm. Eng. Conf., pp. 77–82. DNS data available from the Turbulence and Heat Transfer Laboratory (N. Kasagi) at University of Tokyo, http://www.thtlab.t.u-tokyo.ac.jp/.

[31] Iwamoto, K., Suzuki, Y., and Kasagi, N., 2002. "Reynolds number effect on wall turbulence: Toward effective feedback control". *Int. J. Heat Fluid Flow,* ***23***, pp. 678–689.

Appendix A: Transport Equations for Resolved Turbulent Stresses

In this appendix, the general transport equations for the resolved turbulent stresses in the context of LES of a turbulent flow subjected to a system rotation are systematically derived. The set of transport equations presented here hold also for a non-rotating flow, which can be obtained simply by dropping the terms related to the Coriolis force.

Based on the Reynolds decomposition, an instantaneous filtered quantity can be expressed as:

$$\bar{\phi} = \left[\bar{\phi}\right] + \bar{\phi}'' \tag{15}$$

where the operator $[\cdot]$ represents ensemble-averaging and $\bar{\phi}''$ represents the residual component, with

$$\left[\bar{\phi}''\right] = 0 \tag{16}$$

For the filtered velocity $\bar{u}_i$, the following relationships hold:

$$\bar{u}_i\bar{u}_j = [\bar{u}_i]\,[\bar{u}_j] + [\bar{u}_i]\,\bar{u}_j'' + [\bar{u}_j]\,\bar{u}_i'' + \bar{u}_i''\bar{u}_j'' \tag{17}$$

$$[\bar{u}_i\bar{u}_j] = [\bar{u}_i]\,[\bar{u}_j] + \left[\bar{u}_i''\bar{u}_j''\right] \tag{18}$$

By ensemble-averaging the filtered momentum equation (2), we obtain:

$$\begin{aligned}\frac{\partial\,[\bar{u}_i]}{\partial t} + \frac{\partial}{\partial x_j}([\bar{u}_i\bar{u}_j]) = &-\frac{1}{\rho}\frac{\partial\,[\bar{p}]}{\partial x_i} + \nu\frac{\partial^2\,[\bar{u}_i]}{\partial x_j\partial x_j}\\ &-\frac{\partial\,[\tau_{ij}]}{\partial x_j} + 2\varepsilon_{ij3}\Omega\,[\bar{u}_j]\end{aligned} \tag{19}$$

Substituting Eqns. (17) and (18) into Eqns. (2) and (19), respectively, and then subtracting the resulting equations we get:

$$\begin{aligned}\frac{\partial\bar{u}_i''}{\partial t} + [\bar{u}_j]\,\frac{\partial\bar{u}_i''}{\partial x_j} = &-\bar{u}_j''\frac{\partial\,[\bar{u}_i]}{\partial x_j} - \frac{\partial}{\partial x_j}(\bar{u}_i''\bar{u}_j'' - \left[\bar{u}_i''\bar{u}_j''\right])\\ &-\frac{1}{\rho}\frac{\partial\bar{p}''}{\partial x_i} + \nu\frac{\partial^2\bar{u}_i''}{\partial x_j\partial x_j}\\ &-\frac{\partial(\tau_{ij} - [\tau_{ij}])}{\partial x_j} + 2\varepsilon_{ij3}\Omega\bar{u}_j''\end{aligned} \tag{20}$$

Based on the ensemble-averaging operation, the following transport equation for the resolved turbulent stresses can be obtained from Eqn. (20):

$$\underbrace{\frac{\partial\left[\bar{u}_i''\bar{u}_k''\right]}{\partial t}+\left[\bar{u}_j\right]\frac{\partial\left[\bar{u}_i''\bar{u}_k''\right]}{\partial x_j}}_{\text{I}}=\underbrace{-\left[\bar{u}_i''\bar{u}_j''\right]\frac{\partial\left[\bar{u}_k\right]}{\partial x_j}-\left[\bar{u}_k''\bar{u}_j''\right]\frac{\partial\left[\bar{u}_i\right]}{\partial x_j}}_{\text{II}}$$
$$\underbrace{-\left(\left[\tau_{ij}\frac{\partial\bar{u}_k''}{\partial x_j}\right]+\left[\tau_{kj}\frac{\partial\bar{u}_i''}{\partial x_j}\right]\right)}_{\text{III}}$$
$$\underbrace{+\frac{\partial}{\partial x_j}\left(\left[\bar{u}_i''\tau_{kj}\right]+\left[\bar{u}_k''\tau_{ij}\right]\right)}_{\text{IV}}$$
$$\underbrace{-\frac{\partial}{\partial x_j}\left[\bar{u}_i''\bar{u}_j''\bar{u}_k''\right]}_{\text{V}}$$
$$\underbrace{-\frac{1}{\rho}\left(\left[\bar{u}_i''\frac{\partial\bar{p}''}{\partial x_k}\right]+\left[\bar{u}_k''\frac{\partial\bar{p}''}{\partial x_i}\right]\right)}_{\text{VI}}$$
$$\underbrace{+\nu\left(\left[\bar{u}_i''\frac{\partial^2\bar{u}_k''}{\partial x_j\partial x_j}\right]+\left[\bar{u}_k''\frac{\partial^2\bar{u}_i''}{\partial x_j\partial x_j}\right]\right)}_{\text{VII}}$$
$$\underbrace{+2\Omega\left(\varepsilon_{ij3}\left[\bar{u}_j''\bar{u}_k''\right]+\varepsilon_{kj3}\left[\bar{u}_j''\bar{u}_i''\right]\right)}_{\text{VIII}}\quad(21)$$

The role of each of term in this equation can be identified as follows:
(I) represents the local rate of change and advection by the mean flow of the resolved turbulent shear stress;
(II) represents the production term due to the action of the resolved turbulent stresses on the gradient of the mean velocity, and describes the interaction between the mean and turbulent parts of the flow;
(III) represents the production term due to the action of the SGS stresses on the gradient of the residual velocity, and is associated with the interaction between the SGS stresses and velocity fluctuations;
(IV) is the SGS diffusion term;
(V) is the triple correlation for the fluctuating flow field related to turbulent advection;
(VI) is the velocity-pressure-gradient tensor;
(VII) is the viscous diffusion and dissipation term;
(VIII) represents the production term due to rotation effects.

Equation (21) represents the general transport equation for the resolved turbulent shear stress $[\bar{u}_i''\bar{u}_k'']$. For a plane channel flow, statistics based on time- and plane-averaged quantities (denoted using $\langle\cdot\rangle$) are of more interest to the researcher, because the flow can be further assumed to be: (1) statistically stationary, and (2) homogeneous in the (x_1, x_3)-plane. For LES of a channel flow, an instantaneous filtered quantity can be decomposed into a time- and plane-averaged component and a residual component (see Eqn. (7)). The procedure to derive the transport equation for the turbulent stress $\langle\bar{u}_i''\bar{u}_k''\rangle$ is identical to the procedure used in the derivation of $[\bar{u}_i''\bar{u}_k'']$. However, with these two additional assumptions for a fully-developed plane channel flow, the transport equation for $\langle\bar{u}_i''\bar{u}_k''\rangle$ can be further simplified to give:

$$\begin{aligned}\frac{D\left\langle\bar{u}_i''\bar{u}_k''\right\rangle}{Dt}=0=&-\left\langle\bar{u}_i''\bar{u}_2''\right\rangle\frac{\partial\left\langle\bar{u}_k\right\rangle}{\partial x_2}-\left\langle\bar{u}_k''\bar{u}_2''\right\rangle\frac{\partial\left\langle\bar{u}_i\right\rangle}{\partial x_2}\\&-\left(\left\langle\tau_{ij}\frac{\partial\bar{u}_k''}{\partial x_j}\right\rangle+\left\langle\tau_{kj}\frac{\partial\bar{u}_i''}{\partial x_j}\right\rangle\right)\\&+\frac{\partial}{\partial x_2}\left(\left\langle\bar{u}_i''\tau_{k2}\right\rangle+\left\langle\bar{u}_k''\tau_{i2}\right\rangle\right)\\&-\frac{\partial}{\partial x_2}\left\langle\bar{u}_i''\bar{u}_2''\bar{u}_k''\right\rangle\\&-\frac{1}{\rho}\left(\left\langle\bar{u}_i''\frac{\partial\bar{p}''}{\partial x_k}\right\rangle+\left\langle\bar{u}_k''\frac{\partial\bar{p}''}{\partial x_i}\right\rangle\right)\\&+\nu\left(\left\langle\bar{u}_i''\frac{\partial^2\bar{u}_k''}{\partial x_j\partial x_j}\right\rangle+\left\langle\bar{u}_k''\frac{\partial^2\bar{u}_i''}{\partial x_j\partial x_j}\right\rangle\right)\\&+2\Omega\left(\varepsilon_{ij3}\left\langle\bar{u}_j''\bar{u}_k''\right\rangle+\varepsilon_{kj3}\left\langle\bar{u}_j''\bar{u}_i''\right\rangle\right)\end{aligned}\quad(22)$$

where $D(\cdot)/Dt \overset{\text{def}}{=} \partial(\cdot)/\partial t + \langle u_j\rangle\cdot\partial(\cdot)/\partial x_j$ is the material derivative. In particular, the transport equation for $\langle\bar{u}_1''\bar{u}_2''\rangle$ can be derived from Eqn. (22) as

$$\begin{aligned}\frac{D\left\langle\bar{u}_1''\bar{u}_2''\right\rangle}{Dt}=0=&-\left\langle\bar{u}_2''^2\right\rangle\frac{\partial\left\langle\bar{u}_1\right\rangle}{\partial x_2}\\&-\left(\left\langle\tau_{1j}\frac{\partial\bar{u}_2''}{\partial x_j}\right\rangle+\left\langle\tau_{2j}\frac{\partial\bar{u}_1''}{\partial x_j}\right\rangle\right)\\&+\frac{\partial}{\partial x_2}\left(\left\langle\bar{u}_1''\tau_{22}\right\rangle+\left\langle\bar{u}_2''\tau_{12}\right\rangle\right)-\frac{\partial}{\partial x_2}\left\langle\bar{u}_1''\bar{u}_2''^2\right\rangle\\&-\frac{1}{\rho}\left(\left\langle\bar{u}_1''\frac{\partial\bar{p}''}{\partial x_2}\right\rangle+\left\langle\bar{u}_2''\frac{\partial\bar{p}''}{\partial x_1}\right\rangle\right)\\&+\nu\left(\left\langle\bar{u}_1''\frac{\partial^2\bar{u}_2''}{\partial x_j\partial x_j}\right\rangle+\left\langle\bar{u}_2''\frac{\partial^2\bar{u}_1''}{\partial x_j\partial x_j}\right\rangle\right)\\&+2\Omega\left(\left\langle\bar{u}_2''^2\right\rangle-\left\langle\bar{u}_1''^2\right\rangle\right)\end{aligned}\quad(23)$$

Similarly, the transport equation for the resolved turbulent normal stress $\langle\bar{u}_k''\bar{u}_k''\rangle$ (no summation implied here) can be shown to take the following form:

$$\begin{aligned}\frac{D\left\langle\bar{u}_k''\bar{u}_k''\right\rangle}{Dt}=0=&-2\left\langle\bar{u}_k''\bar{u}_2''\right\rangle\frac{\partial\left\langle\bar{u}_k\right\rangle}{\partial x_2}\\&-2\left\langle\tau_{kj}\frac{\partial\bar{u}_k''}{\partial x_j}\right\rangle+2\frac{\partial\left\langle\bar{u}_k''\tau_{k2}\right\rangle}{\partial x_2}\\&-\frac{\partial}{\partial x_2}\left\langle\bar{u}_2''\bar{u}_k''^2\right\rangle-\frac{2}{\rho}\left\langle\bar{u}_k''\frac{\partial\bar{p}''}{\partial x_k}\right\rangle\\&+2\nu\left\langle\bar{u}_k''\frac{\partial^2\bar{u}_k''}{\partial x_j\partial x_j}\right\rangle\\&+4\Omega\varepsilon_{kj3}\left\langle\bar{u}_j''\bar{u}_k''\right\rangle\end{aligned}\quad(24)$$